ACS Photonics

pubs.acs.org/journal/apchd5

Perspective

Nanophotonic Engineering: A New Paradigm for Spectrally Sensitive Thermal Photodetectors

Jon W. Stewart, Nathaniel C. Wilson, and Maiken H. Mikkelsen*

Cite This: https://dx.doi.org/10.1021/acsphotonics.0c01068

Read Online

ACCESS | Metrics & More | Article Recommendations

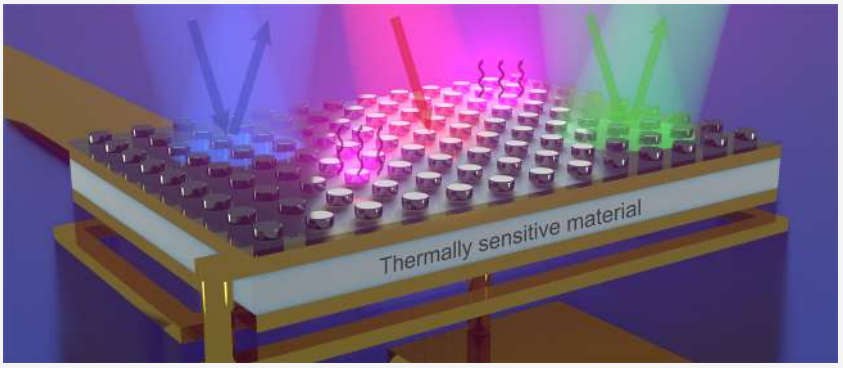

ABSTRACT: Thermal photodetectors rely on thermally sensitive materials to convert the heat generated from incoming light to an electrical signal and are used in, for example, focal plane arrays and for room-temperature, high-photon-flux applications. However, the theory for thermal detectors was initially developed before nanophotonic engineering and, thus, typically assume the integrated absorbers are blackened or have a flat spectral response. Here we discuss recent developments in nanophotonics and metamaterials that have allowed for the creation of spectrally selective absorbers capable of suppressing undesired thermal emission and increasing the potential sensitivity of thermal photodetectors. Furthermore, the subwavelength features of nanophotonic or metamaterial absorbers decrease the amount of material required for absorption, which reduces the detector's thermal capacitance while increasing its response time and sensitivity. The ideal thermal and noise dynamics are derived for both spectrally selective and unselective thermal detectors, revealing exciting opportunities for future thermal photodetectors with increased sensitivities and response times and decreased noise floors.

KEYWORDS: *bolometric, pyroelectric, thermoelectric, spectrally selective, metasurface, nanophotonic*

Photodetectors leveraging thermally sensitive materials integrated with electromagnetic absorbers, such as bolometric, thermoelectric, and pyroelectric detectors, are uniquely capable of sensing light at any wavelength since they solely rely on photothermal conversion; that is, light incident on these thermal detectors is absorbed and converted into heat. The generated heat interacts with a thermally sensitive material converting the heat into an electrical signal. This thermal to electrical conversion is independent of the incident wavelength; as such, the spectral dependence of a thermal detector is solely determined by the absorber. Traditionally, blackened absorbers comprised of thick disordered gold, aluminum, silicon, or carbon films[1−7] are utilized to provide the thermal detectors with a broad sensitivity range covering the visible (VIS) to long-wave infrared (LWIR). Metrology and spectroscopy systems such as FTIRs and laser power meters have found use for the broad sensitivity of thermal detectors; however, the relatively low sensitivity of thermal detectors has discouraged their widespread use when compared to photoconductors (PCs) and photovoltaics/photodiodes (PVs). Development of thermal detectors and associated focal plane arrays (FPAs) has focused on low-cost, room-temperature, and high-photon-flux applications for the LWIR and very long-wave infrared (VLWIR), where thermal detectors can outperform PCs and PVs,[8,9] as well as cryogenic transition edge sensors for submilimeter wave astrophysical applications.[10] However, recent nanophotonic[11−13] and theoretical developments[14] have revealed that thermal detectors with spectrally selective absorbers could outperform their broadband counterparts and even theoretically outper-

Special Issue: 20 Years of Photonics

Received: July 3, 2020
Revised: December 11, 2020
Accepted: December 15, 2020

form PC and PV detectors under specific conditions in the MWIR and beyond.

Here, recent nanophotonic developments and their impact on the sensitivity of thermal detectors are examined to challenge the idea that thermal detectors are less sensitive than PCs and PVs in the VIS to LWIR regime. It should be noted that there is a variety of other promising, emerging detector technologies that include microwave kinetic inductance detectors (MKIDs)[15] and superconducting nanowire single-photon detectors;[16] however, here we will focus our comparison to PCs and PVs due to their commercial relevance for high photon flux applications at noncryogenic temperatures. Much of the thermal detector theory was initially developed in the midtwentieth century,[17−20] which is prior to the development of nanophotonic concepts and tailored thermal emission. Typically, the integrated absorbers are blackened or have a flat spectral response, which not only increases the spectral bandwidth, but also increases the amount of thermal emission. The increased thermal radiation for blackened absorbers increases the thermal conductance away from the thermally sensitive films, which proportionally increases the thermal fluctuation noise and decreases the sensitivity of these photodetectors.

More recently, an idealized thermal detector with a spectrally selective absorber was analytically shown to outperform ideal PCs and PVs for wavelengths beyond the MWIR.[14] To better understand the mechanisms of how nanophotonic absorbers can enhance thermal detectors, the ideal thermal and noise dynamics are derived for both spectrally selective and unselective thermal detectors. The ensuing derivations reveal that the enhancement arises from the primary or secondary reduction in thermal fluctuation noise, thermal capacitance, and thermal conductance, allowing for increased responsivities and decreased noise floors.

NOISE FLOOR FOR IDEAL THERMAL DETECTORS

For an ideal thermal detector, the dominant noise mechanism is assumed to be thermal fluctuation noise resulting from the random exchange of energy between a thermal mass and its surrounding environment. When in thermal equilibrium with the surrounding environment, the thermal noise power in units of watts per $Hz^{0.5}$ is expressed as[9,21,22]

$$\langle P_{th}\rangle = \sqrt{4k_b T^2 G_{th}} \tag{1}$$

where k_b is the Boltzmann constant (1.38×10^{-23} [J·K^{-1}]), T is the temperature, and G_{th} is the thermal conductance between the detector and the environment. The thermal conductance [W/K] is a crucial parameter for thermal detectors and describes the ease at which the thermal energy can flow from the detector to the heat sink. For a fixed operation temperature, the thermal noise power will be minimized when G_{th} is minimized. As such, thermal detectors are typically isolated from their environment by suspension upon thin struts to minimize the heat flow to the environment. Equation 2 shows the thermal conductance for an isolated thermal detector:

$$G_{th} = \frac{1}{R_{th}} = G_{air} + G_{strut} + G_{rad} \tag{2}$$

The thermal conductance of such a detector to its surrounding environment accounts for multiple pathways including the conduction through air, G_{air}, conduction through the struts that suspend and thermally isolate the detector, G_{strut}, and conduction from thermal radiation from the detector to the surrounding environment, G_{rad}. As such, the ideal thermal detector assumes the detectors are in a perfect vacuum and there is no conduction through the isolation legs, that is, $G_{air} = G_{strut} = 0$. The resulting thermal conductance from thermal emission/radiation when in equilibrium with the environment can be estimated with the Stefan−Boltzmann law as follows

$$G_{rad} = \frac{d}{dT}(A\sigma T^4 \eta) = 4A\sigma T^3 \eta \tag{3}$$

where σ is the Stefan−Boltzmann constant (5.67×10^{-8} [W·m^{-2}·K^{-4}]), A is the detector area, and η is the detectors emissivity or absorptivity. This ideal thermal detector theory was derived when blackened, metallic broadband absorbers were standard, and as such, η is assumed to have little spectral dependence. Thus, the minimum detectible power or noise equivalent power (NEP) from an ideal thermal detector is given by eq 4 with units of [W·Hz$^{-0.5}$].

$$\text{NEP} = \frac{\langle P_{th}\rangle}{\eta} = \sqrt{\frac{16k_b T^5 A\sigma}{\eta}} \tag{4}$$

The NEP is a useful parameter for quantifying the magnitude of radiant power incident on the detector that produces an electrical signal equal to the root-mean-square (rms) noise. In other words, the "electrical" NEP is the weakest optical signal that can be detected at the electrical output of a detector for a given bandwidth. It is important to note, there is an ambiguity with the definition of the NEP, which can be specified over the measurement bandwidth or over a "normalized" 1 Hz bandwidth. More specifically, the bandwidth discussed here, represented as Δf, is the electrical bandwidth of the detector and readout circuit, which is commonly referred to as the effective noise bandwidth. If the intrinsic bandwidth of the readout circuit is larger than the integration bandwidth, the electrical bandwidth can be estimated with the Nyquist theorem as $\Delta f = 1/(2t_{avg})$, where t_{avg} is the integration or measurement time. Thus, for the "normalized" 1 Hz bandwidth the electrical signal from the detector will be averaged or integrated for 0.5 s. However, for phase-sensitive readout approaches, such as lock-in amplifiers, the electrical bandwidth can be significantly decreased achieving values as small as $1/(12.8t_{avg})$ for the Stanford Research Systems SR865A amplifier.[23] It is vital for sake of comparison between detectors, that any provided NEP values include a discussion of whether the measurement bandwidth is accounted for in the calculation. In this Article, the NEP will be specified with a 1 Hz bandwidth, and specific detectivity will account for the specific measurement bandwidth of the detector. The normalized or specific detectivity, D^*, is another useful metric, which normalizes a detector's NEP to the area and, in this Article, the measurement bandwidth, Δf. The specific detectivity in units of [cm·Hz$^{0.5}$·W^{-1}] allows for comparison of detectors with different areas and bandwidths, where D^* for the ideal thermal detector is specified as

$$D^* = \frac{\sqrt{A\Delta f}}{\text{NEP}} = \sqrt{\frac{\eta \Delta f}{16k_b T^5 \sigma}} \tag{5}$$

It is worth noting that the specific detectivity was originally formulated for quantum or photovoltaic detectors, where the spectral noise power is proportional to the detector area.

https://dx.doi.org/10.1021/acsphotonics.0c01068
ACS Photonics XXXX, XXX, XXX−XXX

However, noise in thermal detectors does not always follow this scaling trend; for example, temperature fluctuations do not necessarily scale with the detector area when the strut conductance dominates.[24] Thus, D^* should be interpreted cautiously as it tends to overestimate the performance of thermal detectors with larger areas and underestimate the performance of smaller detectors. Notwithstanding, D^* is a useful metric for the general comparison of a detector's sensitivity and, in the case of an ideal thermal detector, does capture the performance well, as temperature fluctuations from thermal emission/radiation scale with area. The specific detectivity of the ideal thermal detector can thus be estimated by assuming Δf = 1 Hz, T = 300 K, and η = 1. Under these conditions, the specific detectivity is 1.81×10^{10} [cm·Hz$^{0.5}$·W^{-1}], which is the maximum specific detectivity for a thermal detector with a broadband absorber if all noise sources apart from thermal fluctuation noise are eliminated. This specific detectivity for the ideal thermal detector is shown in Figure 1

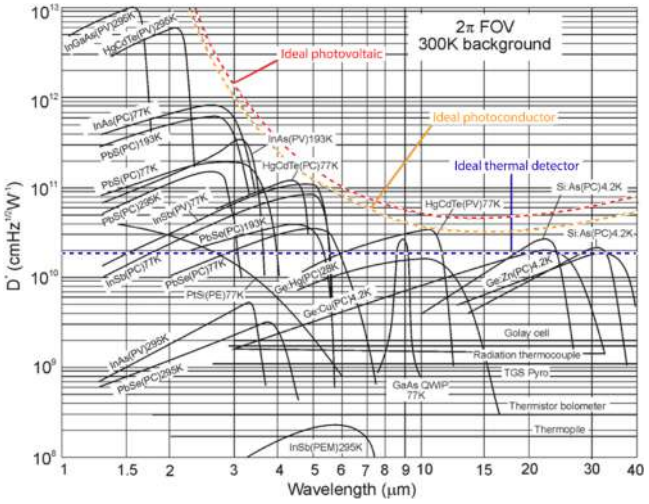

Figure 1. Comparison of the D^* of various available detectors when operated at the indicated temperature. Chopping frequency is 1000 Hz for all detectors except the thermopile (10 Hz), thermocouple (10 Hz), thermistor bolometer (10 Hz), Golay cell (10 Hz), and pyroelectric detector (10 Hz). Each detector is assumed to view a hemispherical surrounding at a temperature of 300 K. Theoretical curves for the background-limited D^* (dashed lines) of ideal photovoltaic and photoconductive detectors and thermal detectors are also shown. PC, photoconductive detector, PV, photovoltaic detector, PEM, photoelectromagnetic detector, and HEB, hot electron bolometer. Reprinted with permission from ref 25. Copyright 2005 American Institute of Physics.

along with the specific detectivities of other experimental and theoretical detectors.[25] From Figure 1, the ideal thermal detector can be seen to have worse performance than ideal PCs or PVs for all wavelengths shown, which has led to the perspective that thermal detectors have poor sensitivities and slow response times due to low thermal conductance. However, as shown previously, the ideal thermal detector derivation assumes a broadband absorber with a unity emissivity over the entire spectral range, which maximizes the thermal conductance from thermal emission for a given temperature. Recent theoretical developments have shown that the specific detectivity of thermal detectors can be substantially improved through integration with spectrally selective absorption and emission filters.[14]

Conveniently, nanophotonic optical materials comprised of highly engineered subwavelength elements have enabled an unprecedented level of control over thermal emission and photothermal conversion.[26−30] By leveraging full control over the thermal emission spectrum, the radiative thermal conductance can be effectively reduced, which would increase the specific detectivity of an ideal, spectrally selective thermal detector. Following a derivation from Talghader et al.,[14] eq 6 below describes the rms energy fluctuations arising from the photon quantization of thermal emission/radiation for a single frequency.

$$\langle (\Delta E)^2 \rangle_f = N(hf)^2 \langle n^2 \rangle = \frac{8\pi h^2 f^4}{c^3} \frac{e^{hf/k_b T}}{(e^{hf/k_b T} - 1)^2} \tag{6}$$

where n is the number of photons in a mode, f is the frequency of the photon, N is the mode density at a given frequency, $\hbar$ is the Planck constant (6.626×10^{-34} [J·s]), and c is the speed of light. By integration over frequency and solid angle, the total rms energy fluctuations from thermal emission can be expressed as[14]

$$\langle (\Delta E) \rangle^2 = \int_{f_1}^{f_2} \int_0^{\pi} \int_0^{2\pi} \frac{2h^2 f^4}{c^3} \times \frac{e^{hf/k_b T}}{(e^{hf/k_b T} - 1)^2} \eta(f, \theta, \varphi) \sin(\theta) \mathrm{d}\varphi \, \mathrm{d}\theta \, \mathrm{d}f \tag{7}$$

Equation 7 allows for the calculation of thermal energy fluctuations $\langle (\Delta E)^2 \rangle^{0.5}$ in units of [J·m^{-1}] from an arbitrary emissivity profile $\eta(f,\theta,\varphi)$ with angular and frequency dependencies. If the detectors are in thermal equilibrium with their surroundings and no substantial temperature changes occur during the measurement, the thermal fluctuations will be stationary. As such, the power spectral density can be calculated according to eq 8 and the specific detectivity according to eq 9:

$$\langle (\Delta P) \rangle^2 = \left\langle \left(\frac{\Delta E}{t_{\mathrm{meas}}} \right) \right\rangle^2 = \langle (2\Delta f \Delta E) \rangle^2 = 4\Delta f^2 \langle (\Delta E) \rangle^2 \tag{8}$$

$$D^* = \sqrt{\frac{\Delta f}{\langle (\Delta P) \rangle^2}} = \sqrt{\frac{1}{4\Delta f \langle (\Delta E) \rangle^2}} \tag{9}$$

where t_{meas} is the integration or measurement time and the measurement bandwidth $\Delta f = 0.5 \cdot t_{\mathrm{meas}}{}^{-1}$. To minimize ΔE and maximize D^*, a nanophotonic absorber for a thermal detector should be designed to absorb only in the desired spectral region and reflect everywhere else. This will reduce the number of absorbed/emitted photons at wavelengths unimportant to the application, which leads to a significantly lower thermal fluctuation noise when compared to a detector absorbing uniformly across the visible and infrared. Assuming a Lambertian thermal emission profile and a square spectral filter with a 1 μm spectral width centered at 10 μm, the specific detectivity would be $\sim 5 \times 10^{10}$ [cm·Hz$^{0.5}$·W^{-1}], which is almost three times more sensitive than the ideal broadband thermal detector. With this simple filter, an ideal spectrally selective thermal detector would outperform ideal PC and PV detectors for wavelengths longer than 10 μm. If the integrated filter is improved to a 100 nm spectral width at 10 μm, the specific detectivity would increase to $\sim 1.4 \times 10^{11}$ [cm·Hz$^{0.5}$·W^{-1}], with the potential to outperform all other detectors for

https://dx.doi.org/10.1021/acsphotonics.0c01068
ACS Photonics XXXX, XXX, XXX−XXX

wavelengths longer than 5 μm. Thus, the traditional notion that thermal detectors have worse sensitivities than PCs or PVs only holds for traditional blackened absorbers. It should be noted that PC and PV detectors can also be constructed with integrated filters, but they do not benefit from the compounded effect of reduced out of band emissivity as thermal detectors do. Updated theories accounting for spectral selectivity and generation-recombination noise show that thermal detectors could outperform other technologies in the MWIR and beyond.

SIMPLE THERMODYNAMIC MODEL FOR THERMAL DETECTORS

Beyond reducing the thermal conductance by spectrally screening unwanted thermal emission, nanophotonic absorbers can further improve thermal detectors by decreasing their thermal capacitance and thus enhancing both the detector's sensitivity and response time. To understand the thermodynamics of these thermal detectors, a simple analytical solution is derived below. While the mechanisms of bolometric, thermoelectric, and pyroelectric detectors are quite different, the thermal design and isolation are similar between approaches, which is illustrated in Figure 2.

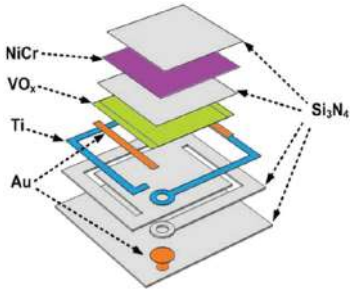

Figure 2. A 25 × 25 μm VO_x microbolometer is shown here, where the resistance of the VO_x changes in response to the temperature of the film. Two thermal isolation struts can be seen along the outside of the detector that connect it to the substrate with 4 μm widths and 50 μm lengths. The Ti and Au conductors are used to electrically contact the thermally sensitive VO_x film (95 nm thick). The 400 nm Si_3N_4 film at the bottom of the heterostructure mechanically supports the structure, and the top Si_3N_4/NiCr/Si_3N_4 stack is the optical absorber with thicknesses of 50/5/50 nm. Reprinted with permission from *AIP Conf. Proc.* **2017**, *1809*, 020001. Copyright 2017 AIP Publishing.

Most thermal detectors consist of a (i) mechanically supporting film for the struts/thermal isolation, (ii) electrical contacts, (iii) a thermally sensitive material, and (iv) an optical absorber. For example, the bolometer in Figure 2 consists of a (i) 400 nm Si_3N_4 supporting film, (ii) a Ti and Au electrical contact, (iii) an 85 nm, thermally sensitive VO_x film, and (iv) an optical absorber from a 50/5/50 nm stack comprised of Si_3N_4/NiCr/Si_3N_4. Equation 10 is the simplest heat balance equation for a passive thermal detector for temperature fluctuations around an equilibrium temperature T. This equation assumes that little to no energy is removed from the system by the thermal to electrical conversion and that there are no influences from the electrical detection method, such as bias currents for bolometric detectors.

$$C_{\mathrm{th}}\frac{\mathrm{d}}{\mathrm{d}t}\Delta T + G_{\mathrm{th}}\Delta T = \eta\Phi \tag{10}$$

where C_{th} is the thermal capacitance, η is the absorption/emissivity for the wavelengths incident upon the detector, and Φ is the radiant power. The thermal capacitance in units of $[\mathrm{J}\cdot\mathrm{K}^{-1}]$ is the capacity of the detector to hold thermal energy and also describes the temperature change of the detector for a given input of energy into the detector. Assuming a periodically varying radiant power or a periodically modulated light source, that is, $\Phi = \Phi_0 e^{i\omega t}$, the amplitude of temperature variation is given by

$$\Delta T = \frac{\eta\Phi_0}{\sqrt{G_{th}^2 + \omega^2 C_{\mathrm{th}}^2}} = \frac{\eta\Phi_0 R_{\mathrm{th}}}{\sqrt{1 + \omega^2\tau_{\mathrm{th}}^2}} \tag{11}$$

where ω is the angular frequency of the modulated light, the thermal resistance is defined as $R_{\mathrm{th}} = 1/G_{\mathrm{th}}$, and the characteristic response time is $\tau_{\mathrm{th}} = C_{\mathrm{th}}/G_{\mathrm{th}}$. The subsequent voltage responsivity, R_{V}, in $[\mathrm{V}\cdot\mathrm{W}^{-1}]$, of the thermal detector is given by

$$R_{\mathrm{V}} = \frac{K_{\mathrm{V}}\Delta T}{\Phi_0} = \frac{\eta K_{\mathrm{V}} R_{\mathrm{th}}}{\sqrt{1 + \omega^2\tau_{\mathrm{th}}^2}} \tag{12}$$

where $K_{\mathrm{V}} = \Delta V/\Delta T$ is the thermal to electrical conversion factor. Equations 11 and 12 illustrate several important features of thermal detectors to maximize ΔT and R_{V} for a given radiant power. In order to maximize the temperature change and responsivity, the thermal capacitance and conductance need to be minimized, while maximizing the absorption for the wavelength of interest. It was shown with eq 7 that an ideal absorber for a thermal detector should perfectly absorb the wavelength of interest and have no absorption otherwise. This allows for complete absorption of the signal while reducing the thermal conductance associated with the thermal emission to the detector's surroundings. As such, in general, thermal detectors should seek the smallest possible detector mass, minimize thermal emission, and utilize the thinnest/longest thermal isolation legs possible to connect the detector to the heat sink.[28] However, further effects also have to be considered, for example, as the strut is made thinner and longer the resistance of the electrical contacts along the struts will increase, which will add Johnson noise to the system and the optimal point of the strut length and width will be specific to the detector design. Similarly, the reduction in the thermal emission will only reduce the noise to the point where the noise arising from the strut conductance again dominates, which will again be specific to the detector design. It should also be noted that thermal conductance may occur not only through radiative effects but also through the support struts. Ideally, the thermal conductance of the detector would be dominated by thermal emission and the strut geometry should be optimized to not add excessive Johnson noise. Gawarikar et al. showed radiation heat transfer dominated microbolometers when the strut conductance was reduced to $\sim 10^{-8}$ W/K. However, this value depends upon the area of the microbolometer, its' spectral response, and associated radiative conductivity. The thermal and strut conductance vary by orders of magnitude between different applications. Depending on the materials used, it is possible that the detector mass could be reduced to the point where thermal fluctuation noise becomes dominant. In the high frequency limit, ΔT is inversely proportional to ω. Thus, the characteristic response time, $\tau_{\mathrm{th}} = C_{\mathrm{th}}/G_{\mathrm{th}}$, is analogous to the RC time constant of an RC (resistor and capacitor) circuit and models the thermally

https://dx.doi.org/10.1021/acsphotonics.0c01068
ACS Photonics XXXX, XXX, XXX−XXX

limited response of the detectors. An optimal thermal detector would have the smallest thermal capacitance possible and the thermal conductance would be engineered to achieve the desired response time and noise floor.

Focusing on the absorber, the use of nanophotonic absorbers due to their subwavelength features and localized absorption can directly reduce the thermal capacitance of the detector, which will result in an increased responsivity and improved thermal response time. Additionally, these absorbers can have a secondary effect of reducing the thermal conductance. Equation 2 showed that the thermal conductance is dependent on the physical design of the detector support structure or the isolation struts, which are designed to provide mechanical support for the electrical contacts, thermally sensitive film, and absorber. As such, if the absorber mass is decreased, the struts can be made thinner and longer due to the reduced mechanical stress. The strut conductance can be modeled as the sum of individual materials comprising the strut as shown below:

$$G_{\text{strut}} = N_{\text{strut}} \sum_i \frac{k_i A_i}{l_i} \tag{13}$$

where N_{strut} is the number of struts isolating the detector, k_i is the thermal conductivity, A_i is the cross-sectional area, and l_i is the length of the strut for the i^{th} material. In most cases, the strut only consists of (i) a low-stress oxide or nitride film acting as the support for the detector structure and (ii) a conductor to electrically contact the thermally sensitive material as shown in Figure 2. For recently demonstrated microbolometers, the struts commonly have thicknesses on the order of 100s of nm, widths on the order of 1s of μm, and lengths in the 10s of μm, resulting in $\sim 10^{-6}$ to 10^{-8} [W·K^{-1}] strut conductances.[31−37] Other than improved fabrication techniques and design, there is little that can be done to reduce the thermal conductance of the strut other than reducing the mechanical stress via reduction in the mass of the suspended detector. This reduction, from integrating a nanophotonic absorber for instance, would allow for the struts to be thinner and longer and thus reducing the thermal conductance and improving the specific detectivity. In a similar form to the thermal conductance, the thermal capacitance can be minimized directly by reducing the mass of the thermal detector. The thermal capacitance can be found from the sum of capacitances for each constituent material:

$$C_{\text{tot}} = \sum_i C_i \tag{14}$$

where $C_i = c_{pi}\rho_i V_i$ is the thermal capacitance of the i^{th} material in the detector heterostructure, which is calculated from the specific heat c_{pi}, the density ρ_i, and the volume V_i for the i^{th} material. The thermal capacitance can be minimized by reducing the mass of the support, contacts, thermally sensitive material, and absorber material, while choosing components with a low specific heat capacity. Any reduction in the mass of the absorber or thermally sensitive material would allow for a concomitant reduction in the mass of the support material, which compounds the reduction in thermal capacitance. Since the absorber and thermal-electrical conversion can be designed separately, each can be optimized independently.

For a specific thermal detection mechanism, such as bolometric, pyroelectric, or thermoelectric detectors, the thermally sensitive elements and contacts can be optimized and effectively fixed to produce the largest responsivities and lowest noise. The thermal to electrical conversion can be optimized according to the NEP and D^* shown below:

$$\text{NEP} = \frac{V_{\text{noise}}}{R_{\text{V}}} = \frac{I_{\text{noise}}}{R_{\text{I}}} \tag{15}$$

$$D^* = \frac{\sqrt{A\Delta f}}{\text{NEP}} = \frac{\sqrt{A\Delta f}}{V_{\text{noise}}} R_{\text{V}} \tag{16}$$

where V_{noise} is the rms voltage noise in [V·Hz$^{-0.5}$] arising from the various noise sources of the thermal detector. Equation 16 demonstrates that the specific detectivity is directly proportional to the responsivity of the detector and inversely proportional to the noise. Since the absorber and thermal-to-electrical-conversion design criteria are assumed to be independent, the thermal to electrical conversion can be optimized by minimization of the NEP through specific geometrical and material selections. In this case, the only further improvement to such a thermal detector is through the absorber design. It should be noted, that with most thermal detectors the electrical bandwidth rather than the thermal bandwidth is chosen to be the limiting bandwidth of the measurement and as such the specific detectivity accounts for the electrical bandwidth of the measurement. If the adverse were true, the excessive electrical bandwidth at higher frequencies than the thermal bandwidth would increase the noise of the measurement adversely impacting the performance of a given thermal detector.

NANOPHOTONIC ABSORBERS INTEGRATED WITH THERMAL DETECTORS

Enhanced absorption strategies for thermal detectors have focused upon integrating thermal detectors into Fabry−Perot cavities,[14,31,38−41] or utilizing plasmonic structures with nanoscale gaps to enhance absorption in highly localized regions.[42] With Fabry−Perot-based absorbers, the thermal detector is typically suspended above a mirrored substrate, where the separation between the thermally isolated detector and the substrate define the resonance wavelength of the filter. These absorbers can readily achieve narrow spectral responses with quality factors (ratio of resonance wavelength to full width half-maximum (fwhm) of the resonance) exceeding 100[43−46] and possess dynamically tunable resonances;[46−50] however, they have a multitude of limitations. First, these filters still require an absorber or lossy material to localize the absorbed optical power in the thermal detector and not the reflective substrate. Second, the absorption in Fabry−Perot cavities can strongly depend on the incident angle necessitating a low-numerical-aperture (NA) imaging system. Third, the area underneath the suspended thermal detector is needed for the Fabry−Perot cavity, prohibiting the placement of supports underneath the thin film, which increases the pixel size and reduces the fill fraction of these detectors for focal plane arrays. Fourth, it is difficult to achieve different spectral responses from neighboring detectors on a single chip, because the spacing of the suspended detectors from the reflective substrate must be independently controlled with nanoscale precision. Lastly, these Fabry−Perot absorbers introduce an additional fundamental noise mechanism into the detector arising from the thermomechanical vibrations of the suspended detector.[40] These unwanted vibrations slightly change the resonance of the Fabry−Perot cavity, altering the absorbed

https://dx.doi.org/10.1021/acsphotonics.0c01068
ACS Photonics XXXX, XXX, XXX−XXX

power at the wavelength of interest and increasing the noise of such detectors. A promising alternative to these Fabry−Perot cavities are nanophotonic or metasurface absorbers which can provide spectral selectivity and enhanced absorption.

Nanophotonic or metasurface absorbers do not suffer from the limitations of the Fabry−Perot based approach as (i) the absorber simultaneously acts as the absorber and spectral filter without the need for an external cavity or any additional thermomechanical noise, (ii) the space beneath the detection element has no optical purpose and can be utilized for folded support structures simultaneously enhancing the thermal properties of the system while enabling a higher device fill fraction, and (iii) the absorptive, spectral, and angle-dependent properties of these materials are largely determined by their geometrical features allowing for any number of different spectral responses to be realized on a single chip. Furthermore, the laterally and vertically structured optical absorbers localize incident electromagnetic energy into significantly subwavelength volumes. This localization allows the volume and mass of a spectrally selective optical absorber to be minimized. For example, a perfect absorber can be realized with an array of holes in a metallic or semiconductor film,[51] where the holes not only improve the ability of the film to absorb incident radiation but also reduce the thermal capacitance of the absorber. Like Fabry−Perot cavities, metasurface absorbers can be designed to be tunable in real time, suggesting that when integrated with a detector, a single detection element could be used for time division multiplexed multispectral sensing.[52−54] Metasurfaces can be split into two main categories: dielectric/semiconductor metasurfaces and metallic/plasmonic metasurfaces. Each thermal detection approach has unique mechanisms responsible for the electrical to thermal conversion, and the integrated absorber must be designed around this mechanism so as not to adversely impact its' performance. Recent demonstrations of nanophotonic absorbers with thermoelectric, bolometric, and pyroelectric detectors are examined in more detail below along with a brief discussion of the detection mechanisms.

Thermoelectric. Thermoelectric detectors operate based on the Seebeck effect (i.e., the thermoelectric effect responsible for conversion of a spatial temperature gradient into an electric potential), which was discovered in 1821 by the physicist Thomas Johann Seebeck.[55] He observed that compass needles would deflect in the presence of a loop comprised of two different metals when a temperature difference was applied between the joints. The Seebeck effect is attributed to the creation of spatial gradients in the number of thermally generated charge carriers due to a temperature gradient across the material. According to Fick's Law, the differing number of thermally excited electrical charges causes diffusion/movement of the charges across the material producing an electric potential and in certain circumstances a thermoelectric current. As an example, if a temperature gradient is established at opposite ends of a copper loop with a uniformly sized wire, the diffusion current will flow equally in both directions around the loop canceling any net thermoelectric current. As such, to establish the generation of athermoelectric current, the electrical symmetry of the detector must be broken. This is typically accomplished with heterojunctions comprised of a single material with abrupt diameter changes,[56] two dissimilar metals,[57,58] or a p−n semiconductor junction.[12,38,59] The Seebeck coefficient with units of $[V{\cdot}K^{-1}]$ is used to describe the generated thermoelectric voltage for a given temperature difference across the material and can be negative or positive depending on the majority charge carrier. For a heterojunction, an effective or relative Seebeck coefficient is specified as the difference between the absolute Seebeck coefficients of the two different materials. Table 1 below lists the absolute Seebeck coefficients for a few different semiconductor and metallic materials.

Table 1. Typical Seebeck Coefficients of a Few Select Thermoelectric Materials[a]

material	Seebeck coefficient $[\mu V{\cdot}K^{-1}]$	refs
Semiconductor		
Si (n-type)	−166−230	9, 60
Si (p-type)	165−236	9, 60
Bi_2Te_3 (n-type)	−84	12
Sb_2Te_3 (p-type)	242	12
PbTe (p-type)	405	61
InAs (n-type)	−140	62
Metal		
Au	1.9−6.5	9, 57
Bi	−72−73.4	9, 57
Sb	48.9	9
Sn	−1.5	63
Ta	−2.4	63
Mo	3.9	63
W	0.9−1.0	9, 63

[a]Some values are single examples in a range as the Seebeck coefficient can depend on doping levels.

Both thermoelectric and thermocouple detectors leverage the Seebeck effect to measure the heat generated from light absorption, where these detectors are designed to measure the temperature difference between the optical absorber and the heat sink or substrate. If multiple thermoelectric or thermocouple junctions are connected in series, often called a thermopile, the generated voltage will increase proportionally to the number of heterojunctions. In the equilibrium case, a thermopile illuminated by a sinusoidally varying optical signal will see a temperature difference ΔT between the heat sink and the detector, according to eq 10. As such, the voltage responsivity of a thermopile detector can be given by modifying eq 12 with the number of heterojunctions, N, as follows:

$$R_V = NK_V\frac{\Delta T}{\Phi_0} = \frac{N\eta\alpha_S R_{th}}{\sqrt{1+\omega^2\tau_{th}^2}} \tag{17}$$

Here the thermal to electrical conversion factor, $K_V = \Delta V/\Delta T$, is the relative Seebeck coefficient of the heterojunctions, α_S. From the previous discussion above, the voltage responsivity will be maximized when the thermal conductance and capacitance are minimized, which can be accomplished with nanophotonic absorbers.

Recent demonstrations of nanophotonic thermoelectric detectors have utilized both dielectric and metallic metasurfaces, depending on the contacting geometry and materials used for the thermoelectric junction.[12,57,64−66] Figure 3 and Table 4 show a few select nanophotonic thermoelectric detectors with different combinations of metallic and semiconductor absorbers and heterojunctions. A thermopile constructed with Au−graphene junctions in a suspended arrangement is illustrated in Figure 3a. For the integrated

https://dx.doi.org/10.1021/acsphotonics.0c01068
ACS Photonics XXXX, XXX, XXX−XXX

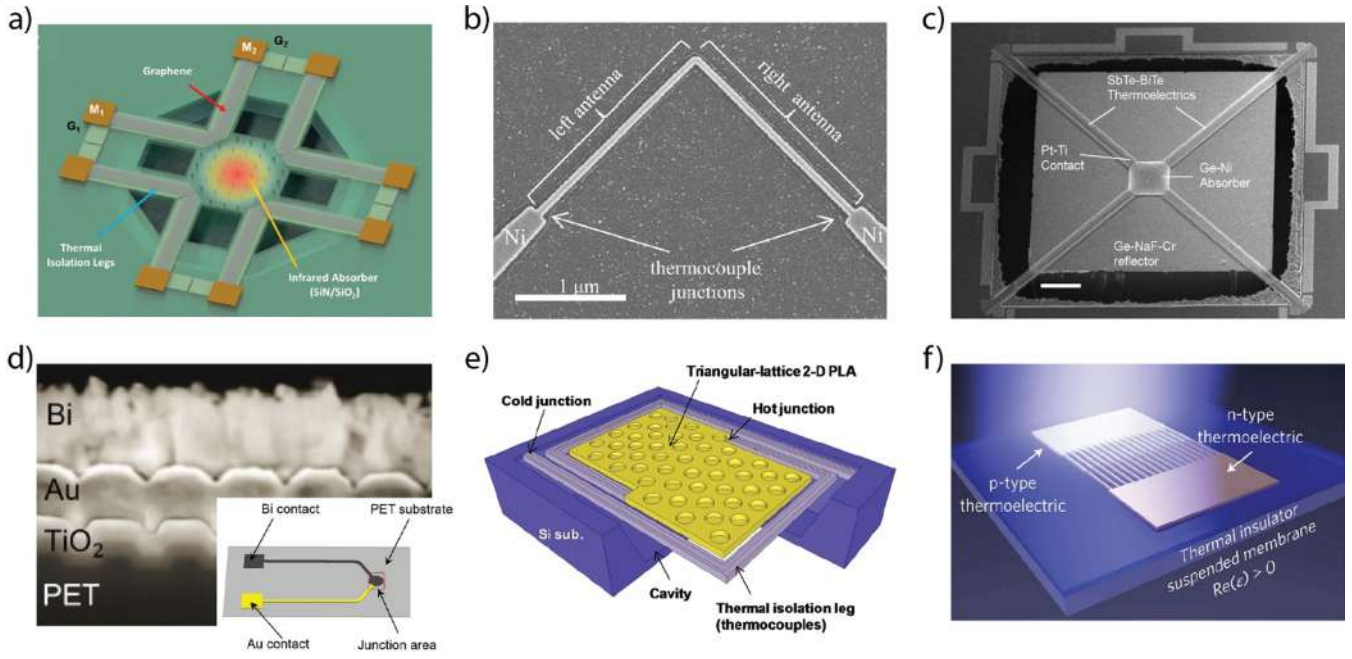

Figure 3. Select thermoelectric and thermocouple detectors with spectrally selective absorbers. (a) Thermopile constructed with Au−graphene junctions with an absorber comprised of a nanohole array in a dielectric Si_3N_4/SiO_2 stack.[58] (b) Thermocouple comprised of a Ni−Ni discontinuity junction, where the shape of the thin Ni wire forms a resonant metallic antenna as the absorber.[56] (c) Thermopile constructed with Sb_2Te_3/Bi_2Te_3 junctions and a thin-film Ge−Ni absorber suspended above a reflective substrate to form a Fabry−Perot cavity.[38] (d) A thermocouple comprised of an Au/Bi junction, where the metals are patterned into a linear grating that facilitates the spectral selectivity and absorption.[57] (e) Thermopile comprised of n-/p-type Si junctions with an absorber made from an array of metallic wells.[59] (f) Thermoelectric detector comprised of Sb_2Te_3/Bi_2Te_3 junctions where the Sb_2Te_3/Bi_2Te_3 junctions are nanostructured to form a linear grating for enhanced absorption.[12] Figure Permissions: (a) Reprinted with permission from ref 58. Copyright 2015 American Chemical Society. (b) Reprinted with permission from *IEEE Trans. Nanotechnol.* **2015**, *14*, 379−383. Copyright 2015 IEEE. (c) Reprinted with permission from *IEEE Trans. Electron Dev.* **2013**, *60*, 2586−2591. Copyright 2013 IEEE. (d) Reprinted with permission from *Adv. Opt. Mater.* **2019**, *7*, 1−8. Copyright 2019 John Wiley and Sons. (e) Reprinted with permission from ref 59. Copyright 2015 MDPI. (f) Reprinted by permission from Springer Nature Customer Service Centre GmbH: Mauser, K. W.; Kim, S.; Mitrovic, S.; Fleischman, D.; Pala, R.; Schwab, K. C.; Atwater, H. A. Resonant Thermoelectric Nanophotonics. *Nat. Nanotechnol.* **2017**, *12*, 770−775. Copyright 2017 Springer.

absorber, a dielectric Si_3N_4/SiO_2 stack patterned into a nanohole array was used with an absorption of ∼50% at 10.6 μm.[58] Variation of the gate bias allowed for tuning of the Seebeck coefficient of graphene and, therefore, the detectivity of the system. This could potentially enable gated detection and enhanced signal-to-noise for some applications. Another example of a thermopile is shown in Figure 3b, which consists of a symmetric pair of Ni antennas coupled to a pair of Ni thermocouples that are realized by a sharp increase in the trace width. The antennas are rotated 90° from one another, which forms a resonant metallic antenna as the absorber and results in polarization-dependent absorption localization. This, in turn, results in a temperature difference between the thermocouples and therefore a photovoltage. The demonstrated detector consisted of nine such pairs connected in series with an estimated specific detectivity of 1.0×10^5 cm·$Hz^{0.5}$·W^{-1}.[56] Figure 3c shows a thermally isolated SbTe-BiTe detector coupled to a Ge−Ni absorber forming the front face of a Fabry−Perot cavity. The SbTe-BiTe thermocouples serve a second purpose as thermally isolating support struts for the absorber. Using a 100 μm × 100 μm absorber, a specific detectivity of 4.4×10^9 cm·$Hz^{0.5}$·W^{-1} was shown.[38] A photonic crystal coupled detector is shown in Figure 3d, which was fabricated using nanoimprint lithography on a polyethylene terephthalate (PET) substrate.[57] This highlights the interesting possibilities of large-scale and inexpensive fabrication strategies as an alternative to traditional electron-beam lithography. Metallic hole arrays have also been used as the absorber structure, for example, coupled to a series of suspended poly-Si thermocouples, as shown in Figure 3e.[59] An example of a plasmonic grating is shown in Figure 3f, where a periodic array of thermoelectric nanowires rest on a suspended dielectric substrate to form the grating structure. This design also leveraged dual purpose elements, as Bi_2Te_3−Sb_2Te_3 served as both the absorber and the thermocouple. This structure enabled the demonstration of spectrally selective absorption combined with a response time of only 341 μs.[12]

Bolometric. Bolometric detectors were first developed by S. P. Langley and by 1880 had been used to measure the solar spectrum, confirming that the peak solar emission occurred where it could be seen visually.[67] Bolometric detectors leverage the dependence of a material's electrical resistivity on temperature to detect absorbed energy, which are commonly comprised of amorphous Si or VO_x thin films. The change in resistance is detected by biasing the bolometer with a current or voltage and measuring the associated change in voltage or current with an increase/decrease in temperature. The temperature coefficient of resistance (TCR), α, is the metric used to characterize how sensitive a bolometric material is to temperature changes and is defined as

$$\alpha = \frac{1}{R}\frac{dR}{dT} \tag{18}$$

https://dx.doi.org/10.1021/acsphotonics.0c01068
ACS Photonics XXXX, XXX, XXX−XXX

The TCR in units of $[\%\cdot K^{-1}]$ or $[K^{-1}]$ is the percentage change of a material's electrical resistance with temperature changes, where R is the electrical resistance. Most materials possess nonzero TCRs due to thermal excitation of electrical carriers and thermal dependence of collision processes; however, very high TCRs can be realized by utilizing superconductors or materials with metal−insulator transitions near their critical temperature. A selection of metallic and semiconductor materials with relatively high TCRs are presented in Table 2.

Table 2. Temperature Coefficients of Resistance (TCR) for Various Materials near Room Temperature[a]

material	TCR $[\%\cdot K^{-1}]$	refs
Semiconductor		
MoS_2 (multiphase)	−2	68
$Si_{0.344}Ge_{0.602}O_{0.054}$	−2.5	69
VWO_x	−2.7−4.1	70
VO_x	−2.0−2.4	71
a-Si	−2.0−3.9	72
$YBa_2Cu_3O_{6+x}$	−2.9−3.5	73
$La_{0.67}Ca_{0.09}Ag_{0.24}MnO_3$	7.5	74
Metal/Semi-Metal		
Ti	0.25−0.29	33, 75
Nb	0.33	76
Bi	−0.35	77
Sb	0.19	77
graphene	4−11	78

[a]Some values are single examples in a range as the TCR can depend on stoichiometry and deposition parameters.

Bolometers can be operated in either constant-current or voltage modes. Assuming a bolometric detector is operated with a constant bias current, I, the detected voltage, ΔV, is given by

$$\Delta V = I\Delta R = IR\alpha\Delta T \tag{19}$$

Utilizing the temperature change for an idealized thermal photodetector under periodic illumination, the temperature change can be inserted in eq 19. However, due to the bias current there is an additional self-heating term $I^2\left(\frac{dR}{dT}\right)$ that must be accounted for. The voltage responsivity of a bolometric detector illuminated with a sinusoidally varying light source is

$$R_V = \frac{IR\alpha\eta}{G_{th} - I^2\left(\frac{dR}{dT}\right) + i\omega C_{th}} = \frac{IR\alpha\eta}{G_{th} - I^2R\alpha + i\omega C_{th}} \tag{20}$$

It should be noted that there is thermal feedback associated with the change in bias current. This feedback can lead to thermal runaway and instabilities in cases of high bias current and positive TCRs.[79,80] For absorbers integrated with bolometric films, it is desirable to localize the current flow predominantly in the bolometric material and minimize leakage currents flowing through the absorber. As such, dielectric absorbers or metasurfaces are most commonly used for bolometric detectors in order to prevent any leakage currents from flowing through the absorber.[13,31,33,39,41,81,82] However, metallic metasurfaces have been integrated with bolometric films either by electrically isolating the metallic absorber with a dielectric film or by utilizing a structured metallic absorber to simultaneously inject current into the

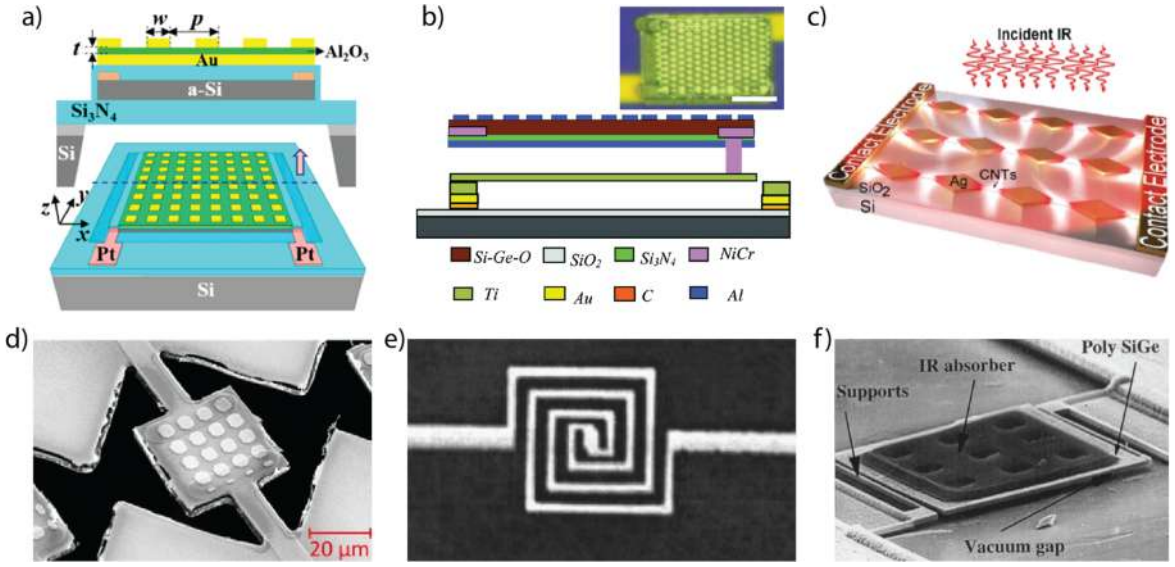

Figure 4. Select bolometric detectors with spectrally selective absorbers. (a) Au metasurface absorber coupled to a thermally isolated a-Si bolometer.[87] (b) Si−Ge−O bolometer with Al metasurface-based absorber and folded thermal isolation supports enabling >90% fill fraction.[69] (c) Carbon nanotube (CNT) bolometer, where the CNTs are selectively grown in the gap of metallic nanoantennas.[88] (d) Au metasurface absorber coupled to a thermally isolated VO_x bolometer.[89] (e) Ni spiral antenna coupled to a thermally isolated Ni microbolometer.[90] (f) $\lambda/4$ absorber coupled to a thermally isolated poly SiGe bolometer.[91] Figure permissions: (a) Reprinted with permission from ref 87. Copyright 2019 MDPI. (b) Reprinted with permission from *2019 20th International Conference on Solid-State Sensors, Actuators and Microsystems and Eurosensors XXXIII, Transducers 2019 and Eurosensors XXXIII* **2019**, 2126−2129. Copyright 2019 IEEE. (c) Reprinted with permission from *Nanotechnology* **2013**, *24* (3), 035502. Copyright 2013 American Institute of Physics. (d) Reprinted with permission from *Infrared Technology and Applications XLII* **2016** *9819*, 98191Q. Copyright 2016 SPIE. (e) Reprinted with permission from *J. Vac. Sci. Technol. B Microelectron. Nanom. Struct.* **2006**, *24* (5), 2356−2359. Copyright 2006 AIP Publishing. (f) Reprinted with permission from *IEEE Transactions on Electron Devices* **1999**, *46* (4), 675−682. Copyright 2019 IEEE.

https://dx.doi.org/10.1021/acsphotonics.0c01068
ACS Photonics XXXX, XXX, XXX−XXX

bolometric film and enhance absorption.[72,83−86] Figure 4 and Table 4 show a few select nanophotonic bolometric detectors with various combinations of metallic and semiconductor absorbers and bolometric films.

Examples of thermally isolated semiconductor bolometers are shown in Figure 4a,b, which are coupled to metallic absorber structures to gain spectral selectivity. The thermally sensitive films are composed of a-Si and Si−Ge−O, respectively, where the example utilizing the Si−Ge−O film observes a high specific detectivity of 5.4×10^8 cm·Hz$^{0.5}$·W^{-1}.[69,87] A novel approach is shown in Figure 4c, where carbon nanotubes were grown in the gap region between diamond-shaped metallic nanoantennas, forming a hybrid absorber−detector structure. In this approach, the plasmonic effects of the nanoantennas were used not only to enhance the absorption of the final structure, but were also used in the fabrication process to enhance the localized growth of carbon nanotubes.[88] In another example, a thermally isolated detector with a VO_x film, shown in Figure 4d, was coupled to a Au metasurface absorber, enabling five resonances from 5.8 to 16.9 μm.[89] Figure 4e shows the simple design of a spiral Ni antenna coupled to a Ni bolometer suspended on an isolating Si_3N_4 film, resulting in a specific detectivity of 1.03×10^8 cm·Hz$^{0.5}$·W^{-1}. The device responsivity was noted to be 164× that of a similar device on a nonsuspended film.[90] A high specific detectivity of 2.3×10^9 cm·Hz$^{0.5}$·W^{-1} was demonstrated with a quarter-wave absorber coupled to a suspended film of polycrystalline SiGe, as shown in Figure 4f. In this case, the performance of the device could potentially be improved further by reducing the high thermal capacitance of the absorber.[91]

Pyroelectric. Pyroelectricity is the phenomena of a crystalline or polycrystalline material that exhibits a temperature-dependent, spontaneous electrical polarization. The pyroelectric effect was initially discovered in the fourth century BCE by the Greek philosopher, Theophrastus, when heated tourmaline crystals attracted pieces of wood, straw, copper, and iron foils.[92,93] When pyroelectric materials are sandwiched between two conductors, the inherent polarization vector, $\boldsymbol{P}_S$ [C·m^{-2}], generates a surface charge density equal to the inherent polarization normal to the surface of the conductors. The pyroelectric coefficient, p, is a metric quantifying the slope of the temperature dependence of the electric displacement field as shown below

$$p = \frac{\mathrm{d}\vec{D}}{\mathrm{d}T} = \frac{\mathrm{d}\vec{P}_S}{\mathrm{d}T} \tag{21}$$

In most cases, the electric field is much smaller than the spontaneous polarization and the pyroelectric coefficient can be written as the temperature derivative of the spontaneous polarization. Since pyroelectric materials are inherently piezoelectric, there can be interplay and cross coupling among thermal, electrical, and mechanical variables. For example, thermally induced strain or thermoelastic coupling can generate an electrical signal through the piezoelectric effect, and secondary or tertiary corrections to the pyroelectric coefficient can be equal to or larger than the primary coefficient for materials such as tourmaline, triglycine sulfate (TGS), and $(CH_2CF_2)_n$. The total pyroelectric coefficient accounting for all other effects on the displacement field from changes in temperature are shown for a few select materials in Table 3.

Table 3. Pyroelectric Coefficients for Various Pyroelectric Materials[a]

material	primary coefficient	secondary coefficient	total coefficient [μC·m^{-2}·K^{-1}]
Ferroelectrics			
$BaTiO_3$	−260	60	−200
$PbZr_{0.95}Ti_{0.05}O_3$	−305.7	37.7	−268
$LiNbO_3$	−95.8	12.8	−83
$LiTaO_3$	−175	−1	−176
$Pb_3Ge_3O_{11}$	−110.5	15.5	−95
$Ba_2NaNb_5O_{15}$	−141.7	41.7	−100
$Sr_{0.5}Ba_{0.5}Nb_2O_6$	−502	−48	−550
$(CH_2CF_2)_n$	−14	−13	−27
triglycine sulfate	60	−330	−270
Nonferroelectrics			
CdSe	−2.94	−0.56	−3.5
CdS	−3.0	−1.0	−4.0
ZnO	−6.9	−2.5	−9.4
tourmaline	−0.48	−3.52	−4.0
$Li_2SO_4·2H_2O$	60.2	26.1	86.3

[a]Values are single examples in a range as the coefficient typically varies with thickness.[93]

The pyroelectric coefficient has units of [μC·m^{-2}·K^{-1}] and can be thought of as the amount of "new" charge generated on the surface of the pyroelectric crystal arising from a 1 K change in temperature for a 1 m^2 area. Once the pyroelectric material is sandwiched between two conductors and connected to an external circuit, a pyroelectric current can be generated when heated or cooled. The pyroelectric current will be proportional to the area of the detector, A, and can be given by

$$i_p = A\frac{\mathrm{d}D}{\mathrm{d}t} = A\frac{\mathrm{d}D}{\mathrm{d}T}\frac{\mathrm{d}T}{\mathrm{d}t} = Ap\frac{\mathrm{d}T}{\mathrm{d}t} \tag{22}$$

Thus, a pyroelectric detector is inherently a current source with a signal proportional to the area, pyroelectric coefficient, and rate of temperature change of the detector. The current responsivity in this case for a sinusoidally modulated light signal can be given by

$$R_i = \frac{i_p}{\Phi_0} = pA\frac{\omega\eta R_{th}}{\sqrt{1+\omega^2\tau_{th}^2}} \tag{23}$$

For low frequencies, $\omega \ll \tau_{th}^{-1}$, the current responsivity is proportional to ω. At frequencies greater than τ_{th}^{-1}, the responsivity asymptotically approaches a constant value, indicating that pyroelectric detectors do not lose sensitivity for higher operation frequencies when compared to bolometric and thermoelectric detectors where the responsivity falls off as ω^{-1} for higher frequencies. However, this derivation assumes that the temperature change of the pyroelectric material occurs instantly upon absorption, when in reality the heat takes time to diffuse through the absorber into the pyroelectric material. As such, the response times of the pyroelectric detectors are inherently bound by the thermal diffusion time from the absorber into the pyroelectric material, which can be on the scale of ns to μs for traditional blackened absorbers. Nanophotonic absorbers, on the other hand, reduce the thermal diffusion time by localizing the absorption close to the pyroelectric material and can show thermal diffusion times in the ps range.[11] Due to the necessity of a conductive contact to the pyroelectric, most recent nanophotonic pyroelectric detectors have utilized metallic metasurfaces as the optical

https://dx.doi.org/10.1021/acsphotonics.0c01068
ACS Photonics XXXX, XXX, XXX−XXX

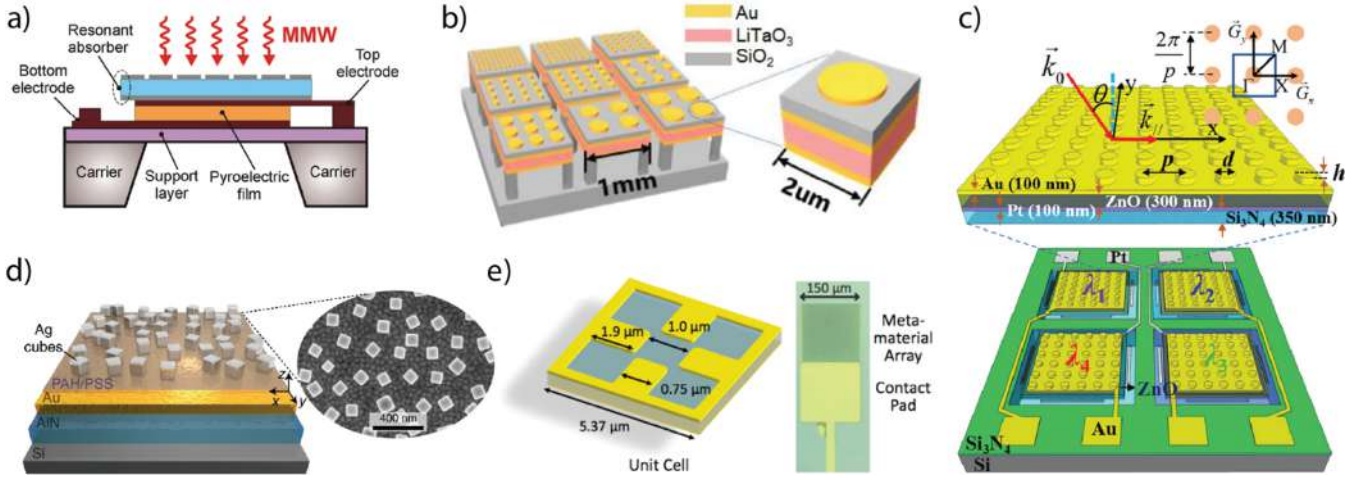

Figure 5. Select pyroelectric detectors with spectrally selective absorbers. (a) Metallic metamaterial optimized for millimeter wave absorption and coupled to a thermally isolated pyroelectric film.[94] (b) Au metasurface absorbers coupled to thermally isolated $LiTaO_2$ films.[95] (c) Quad wavelength Au metasurface absorbers coupled to thermally isolated pyroelectric ZnO films.[96] (d) High-speed detector utilizing metallic absorbers coupled to an AlN pyroelectric film.[11] (e) Au metasurface absorber coupled to thermally isolated $LiNbO_3$ detector.[97] Figure permissions: (a) Reprinted with permission from ref 94. Copyright 2016 Nature. (b) Reprinted with permission from *2018 Conf. Lasers Electro-Optics, CLEO 2018 - Proc.* **2018**, February. Copyright 2018 SPIE. (c) Reprinted with permission from ref 96. Copyright 2019 Wiley. (d) Reprinted with permission from Springer Nature Customer Service Centre GmbH: Stewart, J. W.; Vella, J. H.; Li, W.; Fan, S.; Mikkelsen, M. H. Ultrafast Pyroelectric Photodetection with On-Chip Spectral Filters. *Nature Materials* **2020**, *19*, 158. Copyright 2020 Nature. (e) Reprinted with permission from ref 97. Copyright 2017 The Optical Society.

Table 4. NEP in Units of $[W{\cdot}Hz^{-0.5}]$ and D^* in Units of $[cm{\cdot}Hz^{0.5}{\cdot}W^{-1}]$ for Select Spectrally Selective Thermal Detectors along with Other Relevant Metrics

material	metasurface absorber	wavelength range	response time	device area	NEP	D^*	figure	ref
Thermoelectric								
Ni−Ni (discontinuity)	metallic antenna	10.6 μm		6.1×10^{-7} cm^2		1.0×10^5	3b	56
Au−Bi	metallic grating	550−700 nm		1 cm^2	7.5×10^{-9}		3d	57
Sb_2Te_3−Bi_2Te_3	dielectric grating	600−700 nm	341 μs		8.0×10^{-9}		3f	12
Au−graphene	dielectric hole array	6−14 μm	23 ms	100×100 μm^2			3a	58
N−P type Si	metallic hole array	3−11 μm		300×200 μm^2			3e	59
Sb_2Te_3−Bi_2Te_3	suspended Fabry−Perot cavity	8−12 μm	58 ms	100×100 μm^2	7.2×10^{-13}	4.4×10^9	3c	38
Pyroelectric								
AlN	metallic film-coupled disc array	4−6 μm	122 ms	500×500 μm^2				98
AlN	metallic film-coupled cube array	0.7−2.0 μm	700 ps	$\pi{\cdot}38 \times 38$ μm^2	6.8×10^{-7}	4.0×10^5	5d	11
ZnO	metallic disc array	3−5 μm	153 μs	2×2 mm^2			5c	96
$LiNbO_3$	metallic film-coupled resonator array	8−11 μm	29 ms	150×150 μm^2		9.6×10^6	5e	97
not specified	metallic film-coupled cuboid array	2.14 mm	2.3 ms	$\pi{\cdot}1.3 \times 1.3$ mm^2	2×10^{-9}[a]		5a	94
$LiTaO_3$	metallic film-coupled disc array	2.5−7.5 μm	110 ms	1×1 mm^2			5b	95
Bolometric								
SiGeO	metallic antenna array	8−14 μm	5.3 ms	40×40 μm^2		5.4×10^8	4b	69
carbon nanotubes	metallic antenna	10.6 μm	25 ms	40×40 μm^2		1.0×10^7	4c	88
Ni	spiral antenna	9−11 μm			5.7×10^{-9}	1.0×10^8	4e	90
a-Si	metallic film-coupled cuboid array	3−4 μm		200×200 μm^2			4a	87
VO_x	metallic film-coupled cuboid array	6−18 μm		40×40 μm^2	1.9×10^{-10}		4d	89
SiGe	$\lambda/4$ film	8−14 μm	10 ms	25×25 μm^2		2.3×10^9	4f	91

[a]Denotes estimated rather than measured values.

absorber and electrical contact. Figure 5 and Table 4 show a few select nanophotonic pyroelectric detectors where all demonstrations utilize a metallic absorber to capture the generated pyroelectric charge upon temperature change.

Figure 5a shows the use of a commercial pyroelectric detector adapted to millimeter-wave detection by the addition of a metallic metamaterial absorber structure.[94] An exciting prospect for nanophotonic engineering of thermal detectors is the creation of multispectral arrays. This was demonstrated in the 2.5−7.5 μm range using disk arrays of varying sizes coupled to a pyroelectric $LiTaO_2$ film, as shown in Figure 5b and utilized for gas sensing measurements.[95] A multispectral array was also demonstrated using Au metasurface absorbers coupled to a thermally isolated pyroelectric ZnO film which enabled the detection of four distinct wavelengths in the 3−5 μm range, shown in Figure 5c.[96] In the visible and near-infrared region, a metasurface of plasmonic nanogap structures were utilized to enable resonances at shorter wavelengths from

https://dx.doi.org/10.1021/acsphotonics.0c01068
ACS Photonics XXXX, XXX, XXX−XXX

0.7 to 2.0 μm. As illustrated in Figure 5d, the nanogap structures were formed by either collodial or electron-beam lithography-defined nanocubes coupled to an underlying metal film with a ~10 nm dielectric spacer in between. This entire metasurface structure was then placed on top of an AlN pyroelectric film, effectively acting as both an absorber and an on-chip spectral filter. Due to the short thermal diffusion time associated with the highly subwavelength length scales of the absorber, a high-speed response time of only 700 ps was demonstrated.[11] Figure 5e shows a detector for the 8−11 μm range, where the Au metasurface absorber doubles as a top contact for the pyroelectric $LiNbO_3$ film. By embedding the pyroelectric in the gap between the top contact/metasurface and ground plane, the absorption should be even more localized in the pyroelectric, leading to an improved responsivity.[97]

D and NEP of Nanophotonic Thermal Detectors.* While theoretical developments have shown the capability of ideal thermal detectors to approach $D^* \sim 10^{11}$ [cm·Hz$^{0.5}$·W^{-1}], no practical implementations of spectrally selective thermal detectors have yet to investigate the ultimate sensitivity limits. Recent demonstrations have primarily focused upon integrated spectral filters for reduction in the thermal capacitance of nanophotonic thermal detectors. The specific detectivity and NEP of the nanophotonic thermal detectors included in Figures 3−5 are shown in Table 4, along with the detector's response time, device area, and operational wavelength range.

The highest specific detectivities achieved in Table 4 with spectrally selective thermal detectors is 4.4×10^9 for a suspended Fabry−Perot-based absorber integrated with a thermopile and 2.3×10^9 for a thick $\lambda/4$ antireflection or absorption film integrated with a SiGe bolometer. Commercially available microbolometers have achieved noise equivalent differential temperatures (NETDs) near 20 mK in the LWIR corresponding to a specific detectivity on the order of ~10^8 [cm·Hz$^{0.5}$·W^{-1}].[34,99] Several metasurface thermal detectors do achieve D^* values comparable to these commercially available broadband microbolometers; however, there is much work remaining to investigate the ultimate limits of spectrally selective thermal detectors with detectivities approaching the ~10^{11} [cm·Hz$^{0.5}$·W^{-1}] scale.[100] It should be noted that there is a widespread lack of clarity with respect to the NEP and D^* in many recent demonstrations. It is of critial importance that both NEP and D^* are reported along with sufficient information on the detector's area and the electrical bandwidth of the measurements. Providing accurate characterizations of a detector's performance and sensitivity is paramount,[101] so as to substantiate the improved performance of thermal detectors with nanophotonic absorbers. It would be interesting for future studies to investigate the dependence of NEP and D^* for near-ideal thermal detectors integrated with absorbers of varied spectral widths. One exemplary work demonstrated thermal-radiation-dominated noise with a bolometric detector when the strut conductance was reduced below the conductance of thermal radiation.[31] However, this demonstration lacked an integrated absorber or spectral selectivity, but could provide an interesting platform for investigating the ultimate sensitivity limits of nanophotonic thermal detectors.

PERSPECTIVE

The enhancement of absorption efficiency while reducing thermal capacitance with nanophotonic absorbers is a clear way to improve the performance of thermal photodetectors. Due to their subwavelength features and highly localized absorption, the use of nanophotonic absorbers can directly reduce the thermal capacitance of the detector, which will result in an improved thermal response time and increased responsivity. Additionally, the mass reduction associated with the integration of nanophotonic absorbers enables the use of longer/thinner support structures, which in turn enables a further reduction in the thermal conductance and capacitance of the detector. For applications with specific spectral regions of interest, the thermal radiation/emission in undesired spectral regions can increase the thermal fluctuation noise providing suboptimal performance. Spectrally selective nanophotonic absorbers can be used to suppress emission in undesired spectral regions while enhancing absorption in the desired range. Due to the decreased noise from suppressing undesired thermal radiation, theories suggest that the NEP and specific detectivity can be improved to the point where spectrally selective thermal detectors may outperform their semiconductor counterparts in the MWIR and beyond. Experimental work in this area has been limited providing an interesting opportunity for future studies and efforts. More theoretical and experimental work is needed to establish the practical limits of this enhanced class of thermal detectors. However, a selection of results for spectrally selective thermoelectric, pyroelectric, and bolometric photodetectors presented in Table 4 shows both the promise and room for improvement of these detector types. Spectrally selective thermoelectric and bolometric detectors with thermal isolation have demonstrated specific detectivities in the 10^9 [cm·Hz$^{0.5}$·W^{-1}] range. The highest performing of the representative detectors utilize 1/4 wavelength or Fabry−Perot based absorbers. However, neither approach leverages the full potential reduction in thermal capacitance when compared to nanophotonic or metasurface absorbers; therefore, it may be possible to achieve even higher detectivities. With further experimental and theoretical investigations, these detectors might outperform photovoltaic and photoconductive detectors for wavelengths in the MWIR and beyond. For high-photon-flux applications, such as daylight reflectance imaging or spectral imaging, arrays of spectrally selective thermal detectors may find use for broadband, uncooled multispectral focal plane arrays. Overall, nanophotonic engineering of thermal detectors are a promising platform for constructing uncooled, high-sensitivity and potentially also high-speed devices for a new generation of visible to infrared photodetectors.

AUTHOR INFORMATION

Corresponding Author

Maiken H. Mikkelsen − *Department of Electrical and Computer Engineering, Duke University, Durham, North Carolina 27708, United States;* orcid.org/0000-0002-0487-7585; Email: m.mikkelsen@duke.edu

Authors

Jon W. Stewart − *Department of Electrical and Computer Engineering, Duke University, Durham, North Carolina 27708, United States*

Nathaniel C. Wilson − *Department of Physics, Duke University, Durham, North Carolina 27708, United States*

Complete contact information is available at: https://pubs.acs.org/10.1021/acsphotonics.0c01068

https://dx.doi.org/10.1021/acsphotonics.0c01068
ACS Photonics XXXX, XXX, XXX−XXX

Notes

The authors declare no competing financial interest.

■ ACKNOWLEDGMENTS

Support is acknowledged from the Air Force Office of Scientific Research (AFOSR) Award No. FA9550-18-1-0326. This project is funded in part by the Gordon and Betty Moore Foundation through Grant GBMF8804 to M.H.M. J.W.S. acknowledges support from the Department of Defense (DoD) through the National Defense Science and Engineering Graduate Fellowship (NDSEG).

■ REFERENCES

(1) Christiansen, A. B.; Caringal, G. P.; Clausen, J. S.; Grajower, M.; Taha, H.; Levy, U.; Asger Mortensen, N.; Kristensen, A. Black Metal Thin Films by Deposition on Dielectric Antireflective Moth-Eye Nanostructures. *Sci. Rep.* **2015**, *5*, na DOI: 10.1038/srep10563.

(2) Li, J. M.; Cai, C.; Song, L. X.; Li, J. F.; Zhang, Z.; Xue, M. Z.; Liu, Y. G. Electrodeposition and Characterization of Nano-Structured Black Nickel Thin Films. *Trans. Nonferrous Met. Soc. China* **2013**, *23* (8), 2300−2306.

(3) Zheng, B.; Wang, W.; Jiang, G.; Mei, X. Fabrication of Broadband Antireflective Black Metal Surfaces with Ultra-Light-Trapping Structures by Picosecond Laser Texturing and Chemical Fluorination. *Appl. Phys. B: Lasers Opt.* **2016**, *122* (6), 180.

(4) Pfund, A. H. Bismuth Black and Its Applications. *Rev. Sci. Instrum.* **1930**, *1* (7), 397−399.

(5) Lehman, J.; Theocharous, E.; Eppeldauer, G.; Pannell, C. Gold-Black Coatings for Freestanding Pyroelectric Detectors. *Meas. Sci. Technol.* **2003**, *14* (7), 916−922.

(6) More-Chevalier, J.; Yudin, P. V.; Cibert, C.; Bednyakov, P.; Fitl, P.; Valenta, J.; Novotný, M.; Savinov, M.; Poupon, M.; Zikmund, T.; Poullain, G.; Lančok, J. Black Aluminum-Coated Pt/Pb-(Zr0.56Ti0.44)O3/Pt Thin Film Structures for Pyroelectric Energy Harvesting from a Light Source. *J. Appl. Phys.* **2019**, *126* (21), 214501.

(7) Zabek, D.; Seunarine, K.; Spacie, C.; Bowen, C. Graphene Ink Laminate Structures on Poly(Vinylidene Difluoride) (PVDF) for Pyroelectric Thermal Energy Harvesting and Waste Heat Recovery. *ACS Appl. Mater. Interfaces* **2017**, *9* (10), 9161−9167.

(8) Kruse, P. W. A Comparison of the Limits to the Performance of Thermal and Photon Detector Imaging Arrays. *Infrared Phys. Technol.* **1995**, *36* (5), 869−882.

(9) Rogalski, A. *Infrared and Terahertz Detectors*, 3rd ed.; CRC Press, 2019, DOI: 10.1201/b21951.

(10) Suzuki, A.; Cothard, N.; Lee, A. T.; Niemack, M. D.; Raum, C.; Renzullo, M.; Sasse, T.; Stevens, J.; Truitt, P.; Vavagiakis, E.; Vivalda, J.; Westrook, B.; Yohannes, D. Commercially Fabricated Antenna-Coupled Transition Edge Sensor Bolometer Detectors for next Generation Cosmic Microwave Background Polarimetry Experiment. *J. Low Temp. Phys.* **2020**, *199* (3−4), 1158−1166.

(11) Stewart, J. W.; Vella, J. H.; Li, W.; Fan, S.; Mikkelsen, M. H. Ultrafast Pyroelectric Photodetection with On-Chip Spectral Filters. *Nat. Mater.* **2020**, *19*, 158−162.

(12) Mauser, K. W.; Kim, S.; Mitrovic, S.; Fleischman, D.; Pala, R.; Schwab, K. C.; Atwater, H. A. Resonant Thermoelectric Nanophotonics. *Nat. Nanotechnol.* **2017**, *12* (8), 770−775.

(13) Efetov, D. K.; Shiue, R.-J.; Gao, Y.; Skinner, B.; Walsh, E. D.; Choi, H.; Zheng, J.; Tan, C.; Grosso, G.; Peng, C.; Hone, J.; Fong, K. C.; Englund, D. Fast Thermal Relaxation in Cavity-Coupled Graphene Bolometers with a Johnson Noise Read-Out. *Nat. Nanotechnol.* **2018**, *13* (9), 797−801.

(14) Talghader, J. J.; Gawarikar, A. S.; Shea, R. P. Spectral Selectivity in Infrared Thermal Detection. *Light: Sci. Appl.* **2012**, *1* (8), e24−e24.

(15) Mazin, B.; Bailey, J.; Bartlett, J.; Bockstiegel, C.; Bumble, B.; Coiffard, G.; Currie, T.; Daal, M.; Davis, K.; Dodkins, R.; Fruitwala, N.; Jovanovic, N.; Lipartito, I.; Lozi, J.; Males, J.; Mawet, D.; Meeker, S.; O'Brien, K.; Rich, M.; Smith, J.; Steiger, S.; Swimmer, N.; Walter, A.; Zobrist, N.; Zmuidzinas, J. MKIDs in the 2020s; Astro2020: Decadal Survey on Astronomy and Astrophysics, APC white papers. *Bulletin of the American Astronomical Society* **2019**, *51*, 17.

(16) You, L. Superconducting Nanowire Single-Photon Detectors for Quantum Information. *Nanophotonics* **2020**, *9* (9), 2673−2692.

(17) Jones, R. C. The Ultimate Sensitivity of Radiation Detectors. *J. Opt. Soc. Am.* **1947**, *37* (11), 879−890.

(18) Lewis, W. B. Fluctuations in Streams of Thermal Radiation. *Proc. Phys. Soc.* **1947**, *59* (1), 34−40.

(19) Wormser, E. M. Properties of Thermistor Infrared Detectors. *J. Opt. Soc. Am.* **1953**, *43* (1), 15.

(20) Golay, M. J. E. The Theoretical and Practical Sensitivity of the Pneumatic Infra-Red Detector. *Rev. Sci. Instrum.* **1949**, *20* (11), 816−820.

(21) Rogalski, A. Infrared Detectors: An Overview. *Infrared Phys. Technol.* **2002**, *43* (3−5), 187−210.

(22) Rogalski, A.; Antoszewski, J.; Faraone, L. Third-Generation Infrared Photodetector Arrays. *J. Appl. Phys.* **2009**, *105* (9), 091101.

(23) Stanford Research Systems. Lock-In Amplifier SR865A.

(24) Datskos, P. G. Detectors: Figures of Merit. *Encyclopedia of Optical and Photonic Engineering*, 2nd ed.; CRC Press, 2015; pp 1−9, DOI: 10.1081/E-EOE2-120009723.

(25) Rogalski, A. HgCdTe Infrared Detector Material: History. *Rep. Prog. Phys.* **2005**, *68* (10), 2267−2336.

(26) Raman, A. P.; Anoma, M. A.; Zhu, L.; Rephaeli, E.; Fan, S. Passive Radiative Cooling below Ambient Air Temperature under Direct Sunlight. *Nature* **2014**, *515* (7528), 540−544.

(27) Kou, J. l.; Jurado, Z.; Chen, Z.; Fan, S.; Minnich, A. J. Daytime Radiative Cooling Using Near-Black Infrared Emitters. *ACS Photonics* **2017**, *4* (3), 626−630.

(28) Zhai, Y.; Ma, Y.; David, S. N.; Zhao, D.; Lou, R.; Tan, G.; Yang, R.; Yin, X. Scalable-Manufactured Randomized Glass-Polymer Hybrid Metamaterial for Daytime Radiative Cooling. *Science (Washington, DC, U. S.)* **2017**, *355* (6329), 1062−1066.

(29) Li, W.; Shi, Y.; Chen, Z.; Fan, S. Photonic Thermal Management of Coloured Objects. *Nat. Commun.* **2018**, *9* (1), 4240.

(30) Coppens, Z. J.; Valentine, J. G. Spatial and Temporal Modulation of Thermal Emission. *Adv. Mater.* **2017**, *29* (39), 1701275.

(31) Gawarikar, A. S.; Shea, R. P.; Mehdaoui, A.; Talghader, J. J. Radiation Heat Transfer Dominated Microbolometers. *2008 IEEE/LEOS International Conference on Optical MEMs and Nanophotonics*; IEEE, 2008; pp 178−179, DOI: 10.1109/OMEMS.2008.4607887.

(32) Middleton, C. F.; Boreman, G. D. Technique for Thermal Isolation of Antenna-Coupled Infrared Microbolometers. *J. Vac. Sci. Technol. B Microelectron. Nanom. Struct.* **2006**, *24* (5), 2356.

(33) Bhan, R. K.; Saxena, R. S.; Jalwani, C. R.; Lomash, S. K. Uncooled Infrared Microbolometer Arrays and Their Characterisation Techniques. *Def. Sci. J.* **2009**, *59* (6), 580−589.

(34) Rogalski, A. Next Decade in Infrared Detectors. In *Electro-Optical and Infrared Systems: Technology and Applications XIV*; Huckridge, D. A., Ebert, R., Bürsing, H., Eds.; SPIE, 2017; p 100, DOI: 10.1117/12.2300779.

(35) Deng, Y. Z.; Tang, S. F.; Zeng, H. Y.; Wu, Z. Y.; Tung, D. K. Experiments on Temperature Changes of Microbolometer under Blackbody Radiation and Predictions Using Thermal Modeling by COMSOL Multiphysics Simulator. *Sensors* **2018**, *18* (8), 2593.

(36) Schoeman, J.; du Plessis, M. Recent Advances in the Modelling of the Thermal Conductance of Uncooled Microbolometers. *Proc. SPIE* **2016**, *10036* (February 2017), 100360B.

(37) Tanrikulu, M. Y.; Okyay, A. K.; Yildizak, C.; Akin, T.; Akar, O.; Sarac, A. Single Layer Microbolometer Detector Pixel Using ZnO Material. In *Proceedings of SPIE*; Fulop, G. F., Hanson, C. M., Norton, P. R., Andresen, B. F., Miller, J. L., Eds.; SPIE, 2018; Vol. *1062417*, p 46, DOI: 10.1117/12.2302996.

(38) Gawarikar, A. S.; Shea, R. P.; Talghader, J. J. High Detectivity Uncooled Thermal Detectors with Resonant Cavity Coupled Absorption in the Long-Wave Infrared. *IEEE Trans. Electron Devices* **2013**, *60* (8), 2586−2591.

https://dx.doi.org/10.1021/acsphotonics.0c01068
ACS Photonics XXXX, XXX, XXX−XXX

(39) Wang, Y.; Potter, B. J.; Talghader, J. J. Coupled Absorption Filters for Thermal Detectors. *Opt. Lett.* **2006**, *31* (13), 1945.
(40) Talghader, J. J. Thermal and Mechanical Phenomena in Micromechanical Optics. *J. Phys. D: Appl. Phys.* **2004**, *37* (10), 109.
(41) Song, W.-B.; Talghader, J. J Design and Characterization of Adaptive Microbolometers. *J. Micromech. Microeng.* **2006**, *16* (5), 1073−1079.
(42) Qi, Z.; Zhai, Y.; Wen, L.; Wang, Q.; Chen, Q.; Iqbal, S.; Chen, G.; Xu, J.; Tu, Y. Au Nanoparticle-Decorated Silicon Pyramids for Plasmon-Enhanced Hot Electron near-Infrared Photodetection. *Nanotechnology* **2017**, *28* (27), 275202.
(43) Kim, C. K.; Lee, M. L.; Jun, C.-H.; Choi, C. A. Monolithic Fabry−Perot Wavelength Tunable Filter with Electrothermal Actuation. *Jpn. J. Appl. Phys.* **2005**, *44* (2), 905−909.
(44) Strassner, M.; Simozrag, B.; Bouchoule, S.; Sagnes, I. Widely Tunable and Highly Selective Monolithic Fabry-Perot Filter for Dense WDM Systems. *2005 IEEE LEOS Annual Meeting Conference Proceedings*; IEEE, 2005; Vol. *2005*, pp 287−288, DOI: 10.1109/LEOS.2005.1547983.
(45) Chitica, N.; Daleiden, J.; Strassner, M.; Streubel, K. Monolithic InP-Biased Tunable Filter with 10-Nm Bandwidth for Optical Data Interconnects in the 1550-Nm Band. *IEEE Photonics Technol. Lett.* **1999**, *11* (5), 584−586.
(46) Rissanen, A.; Kantojärvi, U.; Blomberg, M.; Antila, J.; Eränen, S. Monolithically Integrated Microspectrometer-on-Chip Based on Tunable Visible Light MEMS FPI. *Sens. Actuators, A* **2012**, *182*, 130−135.
(47) Neumann, N. Tunable Infrared Detector with Integrated Micromachined Fabry-Perot Filter. *J. Micro/Nanolithogr., MEMS, MOEMS* **2008**, *7* (2), 021004.
(48) Blomberg, M.; Kattelus, H.; Miranto, A. Electrically Tunable Surface Micromachined Fabry-Perot Interferometer for Visible Light. *Sens. Actuators, A* **2010**, *162*, 184−188.
(49) Meinig, M.; Kurth, S.; Seifert, M.; Hiller, K.; Wecker, J.; Ebermann, M.; Neumann, N.; Gessner, T. Tunable Fabry-Pérot Interferometer with Subwavelength Grating Reflectors for MWIR Microspectrometers. In *Advanced Fabrication Technologies for Micro/Nano Optics and Photonics IX*; von Freymann, G., Schoenfeld, W. V., Rumpf, R. C., Eds.; International Society for Optics and Photonics, 2016; Vol. *9759*, p 97590W, DOI: 10.1117/12.2213647.
(50) Ebermann, M.; Neumann, N.; Hiller, K.; Seifert, M.; Meinig, M.; Kurth, S. Tunable MEMS Fabry-Pérot Filters for Infrared Microspectrometers: A Review. *Proc. SPIE* **2016**, *9760*, 97600H.
(51) Dao, T. D.; Ishii, S.; Yokoyama, T.; Sawada, T.; Sugavaneshwar, R. P.; Chen, K.; Wada, Y.; Nabatame, T.; Nagao, T. Hole Array Perfect Absorbers for Spectrally Selective Midwavelength Infrared Pyroelectric Detectors. *ACS Photonics* **2016**, *3* (7), 1271−1278.
(52) Yao, Y.; Shankar, R.; Kats, M. A.; Song, Y.; Kong, J.; Loncar, M.; Capasso, F. Electrically Tunable Metasurface Perfect Absorbers for Ultrathin Mid-Infrared Optical Modulators. *Nano Lett.* **2014**, *14* (11), 6526−6532.
(53) Peng, J.; Jeong, H.-H.; Lin, Q.; Cormier, S.; Liang, H.-L.; De Volder, M. F. L.; Vignolini, S.; Baumberg, J. J. Scalable Electrochromic Nanopixels Using Plasmonics. *Sci. Adv.* **2019**, *5*, eaaw2205.
(54) Hoang, T. B.; Mikkelsen, M. H. Broad Electrical Tuning of Plasmonic Nanoantennas at Visible Frequencies. *Appl. Phys. Lett.* **2016**, *108* (18), 183107.
(55) Seebeck, T. J. Ueber Die Magnetische Polarisation Der Metalle Und Erze Durch Temperatur-Differenz. *Ann. Phys.* **1826**, *82* (2), 133−160.
(56) Szakmany, G. P.; Orlov, A. O.; Bernstein, G. H.; Porod, W. Novel Nanoscale Single-Metal Polarization-Sensitive Infrared Detectors. *IEEE Trans. Nanotechnol.* **2015**, *14* (2), 379−383.
(57) Monshat, H.; Liu, L.; Lu, M. A Narrowband Photo-Thermoelectric Detector Using Photonic Crystal. *Adv. Opt. Mater.* **2019**, *7* (3), 1−8.
(58) Hsu, A. L.; Herring, P. K.; Gabor, N. M.; Ha, S.; Shin, Y. C.; Song, Y.; Chin, M.; Dubey, M.; Chandrakasan, A. P.; Kong, J.; Jarillo-Herrero, P.; Palacios, T. Graphene-Based Thermopile for Thermal Imaging Applications. *Nano Lett.* **2015**, *15* (11), 7211−7216.
(59) Takagawa, Y.; Ogawa, S.; Kimata, M. Detection Wavelength Control of Uncooled Infrared Sensors Using Two-Dimensional Lattice Plasmonic Absorbers. *Sensors* **2015**, *15* (6), 13660−13669.
(60) Mancarella, F.; Roncaglia, A.; Cardinali, G. C. A Measurement Technique for Thermoelectric Power of CMOS Layers at the Wafer Level. *Sens. Actuators, A* **2006**, *132* (1), 289−295.
(61) Crocker, A. J.; Rogers, L. M. Interpretation of the Hall Coefficient, Electrical Resistivity and Seebeck Coefficient of p-Type Lead Telluride. *Br. J. Appl. Phys.* **1967**, *18* (5), 563−573.
(62) Schmidt, V.; Mensch, P. F. J.; Karg, S. F.; Gotsmann, B.; Das Kanungo, P.; Schmid, H.; Riel, H. Using the Seebeck Coefficient to Determine Charge Carrier Concentration, Mobility, and Relaxation Time in InAs Nanowires. *Appl. Phys. Lett.* **2014**, *104* (1), 012113.
(63) Fiflis, P.; Kirsch, L.; Andruczyk, D.; Curreli, D.; Ruzic, D. Seebeck Coefficient Measurements on Li, Sn, Ta, Mo, and W. *J. Nucl. Mater.* **2013**, *438* (1−3), 224−227.
(64) Zolotavin, P.; Evans, C.; Natelson, D. Photothermoelectric Effects and Large Photovoltages in Plasmonic Au Nanowires with Nanogaps. *J. Phys. Chem. Lett.* **2017**, *8* (8), 1739−1744.
(65) Russer, J. A.; Jirauschek, C.; Szakmany, G. P.; Schmidt, M.; Orlov, A. O.; Bernstein, G. H.; Porod, W.; Lugli, P.; Russer, P. A Nanostructured Long-Wave Infrared Range Thermocouple Detector. *IEEE Trans. Terahertz Sci. Technol.* **2015**, *5* (3), 335−343.
(66) Pan, Y.; Tagliabue, G.; Eghlidi, H.; Höller, C.; Dröscher, S.; Hong, G.; Poulikakos, D. A Rapid Response Thin-Film Plasmonic-Thermoelectric Light Detector. *Sci. Rep.* **2016**, *6*, na DOI: 10.1038/srep37564.
(67) Langley, S. P. The Bolometer and Radiant Energy. *Proc. Am. Acad. Arts Sci.* **1880**, *16*, 342.
(68) Kim, J. S.; Kim, J.; Zhao, J.; Kim, S.; Lee, J. H.; Jin, Y.; Choi, H.; Moon, B. H.; Bae, J. J.; Lee, Y. H.; Lim, S. C. Electrical Transport Properties of Polymorphic MoS2. *ACS Nano* **2016**, *10*, 7500.
(69) Alkorjia, O.; Abdullah, A.; Koppula, A.; Warder, C.; Liu, T.; Qu, C.; Zhu, C.; Kinzel, E.; Almasri, M. Metasurface Based Uncooled Microbolometer with High Fill Factor. *2019 20th International Conference on Solid-State Sensors, Actuators and Microsystems and Eurosensors XXXIII, Transducers 2019 and Eurosensors XXXIII*; Institute of Electrical and Electronics Engineers Inc., 2019; pp 2126−2129, DOI: 10.1109/transducers.2019.8808619.
(70) Chi-Anh, N.; Shin, H. J.; Kim, K.; Han, Y. H.; Moon, S. Characterization of Uncooled Bolometer with Vanadium Tungsten Oxide Infrared Active Layer. *Sens. Actuators, A* **2005**, *123-124*, 87−91.
(71) Wang, H.; Yi, X.; Huang, G.; Xiao, J.; Li, X.; Chen, S. IR Microbolometer with Self-Supporting Structure Operating at Room Temperature. *Infrared Phys. Technol.* **2004**, *45* (1), 53−57.
(72) Wu, Y.; Qu, Z.; Osman, A.; Cao, W.; Khokhar, A. Z.; Soler Penades, J.; Muskens, O. L.; Mashanovich, G. Z.; Nedeljkovic, M. Mid-Infrared Nanometallic Antenna Assisted Silicon Waveguide Based Bolometers. *ACS Photonics* **2019**, *6* (12), 3253−3260.
(73) Dayeh, S. A.; Butler, D. P.; Çelik-Butler, Z. Micromachined Infrared Bolometers on Flexible Polyimide Substrates. *Sens. Actuators, A* **2005**, *118* (1), 49−56.
(74) Chu, K.; Sun, T.; Liu, Y.; Dong, G.; Zhang, S.; Li, H.; Pu, X. R.; Yu, X.; Liu, X. Enhanced Room Temperature Coefficient of Resistivity (RT-TCR) and Broad Metal-Insulator Transition Temperature (TMI) of La0.67Ca0.33-XAgxMnO3 Polycrystalline Ceramics. *Ceram. Int.* **2019**, *45* (14), 17073−17080.
(75) Saxena, R. S.; Bhan, R. K.; Rana, P. S.; Vishwakarma, A. K.; Aggarwal, A.; Khurana, K.; Gupta, S. Study of Performance Degradation in Titanium Microbolometer IR Detectors Due to Elevated Heating. *Infrared Phys. Technol.* **2011**, *54* (4), 343−352.
(76) Nolen, S.; Koch, J. A.; Paulter, N. G.; Reintsema, C. D.; Grossman, E. N. Antenna-Coupled Niobium Bolometers for Millimeter-Wave Imaging Arrays. *Proc. SPIE* **1999**, *3795* (November), 279.

https://dx.doi.org/10.1021/acsphotonics.0c01068
ACS Photonics XXXX, XXX, XXX−XXX

(77) Block, W. H.; Gaddy, O. L. Thin Metal Film Room-Temperature IR Bolometers With Nanosecond Response Time. *IEEE J. Quantum Electron.* **1973**, *9* (11), 1044−1053.
(78) Sassi, U.; Parret, R.; Nanot, S.; Bruna, M.; Borini, S.; De Fazio, D.; Zhao, Z.; Lidorikis, E.; Koppens, F. H. L.; Ferrari, A. C.; Colli, A. Graphene-Based Mid-Infrared Room-Temperature Pyroelectric Bolometers with Ultrahigh Temperature Coefficient of Resistance. *Nat. Commun.* **2017**, *8*, na DOI: 10.1038/ncomms14311.
(79) Richards, P. L. Bolometers for Infrared and Millimeter Waves. *J. Appl. Phys.* **1994**, *76* (1), 1−24.
(80) Kraus, H. Superconductive Bolometers and Calorimeters. *Supercond. Sci. Technol.* **1996**, *9*, 827.
(81) Niklaus, F.; Vieider, C.; Jakobsen, H. MEMS-Based Uncooled Infrared Bolometer Arrays: A Review. *Proc. SPIE* **2007**, *6836* (January), 68360D.
(82) Chen, C.; Zhou, Z. Optical Phonons Assisted Infrared Absorption in v O2 Based Bolometer. *Appl. Phys. Lett.* **2007**, *91* (1), 11107.
(83) Niesler, F. B. P.; Gansel, J. K.; Fischbach, S.; Wegener, M. Metamaterial Metal-Based Bolometers. *Appl. Phys. Lett.* **2012**, *100* (20), 203508.
(84) Tucker, E.; D'Archangel, J.; Raschke, M.; Briones, E.; Javier González, F.; Boreman, G. Near-Field Mapping of Dipole Nano-Antenna-Coupled Bolometers. *J. Appl. Phys.* **2013**, *114* (3), 33109.
(85) Maier, T.; Brückl, H. Wavelength-Tunable Microbolometers with Metamaterial Absorbers. *Opt. Lett.* **2009**, *34* (19), 3012.
(86) Denis, K. L.; Cao, N. T.; Chuss, D. T.; Eimer, J.; Hinderks, J. R.; Hsieh, W. T.; Moseley, S. H.; Stevenson, T. R.; Talley, D. J.; U-Yen, K.; Wollack, E. J.; et al. Fabrication of an Antenna-Coupled Bolometer for Cosmic Microwave Background Polarimetry. *AIP Conf. Proc.* **2009**, *1185*, 371−374.
(87) Dao, T. D.; Doan, A. T.; Ishii, S.; Yokoyama, T.; Ørjan, H. S.; Ngo, D. H.; Ohki, T.; Ohi, A.; Wada, Y.; Niikura, C.; Miyajima, S.; Nabatame, T.; Nagao, T. MEMS-Based Wavelength-Selective Bolometers. *Micromachines* **2019**, *10* (6), 416.
(88) Mahjouri-Samani, M.; Zhou, Y. S.; He, X. N.; Xiong, W.; Hilger, P.; Lu, Y. F. Plasmonic-Enhanced Carbon Nanotube Infrared Bolometers. *Nanotechnology* **2013**, *24* (3), 035502.
(89) Smith, E. M.; Nath, J.; Ginn, J.; Peale, R. E.; Shelton, D. Responsivity Improvements for a Vanadium Oxide Microbolometer Using Subwavelength Resonant Absorbers. In *Infrared Technology and Applications XLII*; Andresen, B. F., Fulop, G. F., Hanson, C. M., Miller, J. L., Norton, P. R., Eds.; 2016; Vol. *9819*, p 98191Q. .
(90) Middleton, C. F.; Boreman, G. D. Technique for Thermal Isolation of Antenna-Coupled Infrared Microbolometers. *J. Vac. Sci. Technol. B Microelectron. Nanom. Struct.* **2006**, *24* (5), 2356−2359.
(91) Sedky, S.; Fiorini, P.; Baert, K.; Hermans, L.; Mertens, R. Characterization and Optimization of Infrared Poly SiGe Bolometers. *IEEE Trans. Electron Devices* **1999**, *46* (4), 675−682.
(92) Lang, S. B. The History of Pyroelectricity: From Ancient Greece to Space Missions. *Ferroelectrics* **1999**, *230* (1), 99−108.
(93) Lang, S. B. Pyroelectricity: From Ancient Curiosity to Modern Imaging Tool. *Phys. Today* **2005**, *58* (8), 31−36.
(94) Kuznetsov, S. A.; Paulish, A. G.; Navarro-Ciá, M.; Arzhannikov, A. V. Selective Pyroelectric Detection of Millimetre Waves Using Ultra-Thin Metasurface Absorbers. *Sci. Rep.* **2016**, *6* (January), 1−11.
(95) Tan, X.; Li, J.; Yang, A.; Liu, H.; Yi, F. Narrowband Plasmonic Metamaterial Absorber Integrated Pyroelectric Detectors towards Infrared Gas Sensing. *2018 Conference on Lasers and Electro-Optics, CLEO 2018 - Proceedings* **2018**, 53.
(96) Dao, T. D.; Ishii, S.; Doan, A. T.; Wada, Y.; Ohi, A.; Nabatame, T.; Nagao, T. An On-Chip Quad-Wavelength Pyroelectric Sensor for Spectroscopic Infrared Sensing. *Adv. Sci.* **2019**, *6* (20), 1900579.
(97) Suen, J. Y.; Fan, K.; Montoya, J.; Bingham, C.; Stenger, V.; Sriram, S.; Padilla, W. J. Multifunctional Metamaterial Pyroelectric Infrared Detectors. *Optica* **2017**, *4* (2), 276.
(98) Yamamoto, K.; Goericke, F.; Guedes, A.; Jaramillo, G.; Hada, T.; Pisano, A. P.; Horsley, D. Pyroelectric Aluminum Nitride Micro Electromechanical Systems Infrared Sensor with Wavelength-Selective Infrared Absorber. *Appl. Phys. Lett.* **2014**, *104* (11), 111111.
(99) Rogalski, A.; Sizov, F. F.; Gumenjuk-Sichevska, J. V.; Kostyukevych, S. A. Competition of Infrared Detector Technologies. *Proc. SPIE* **2002**, *5065*, 23.
(100) Talghader, J. J.; Gawarikar, A. S.; Shea, R. P. Beyond the Blackbody Radiation Limit: High-Sensitivity Thermal Detectors. *Proc. SPIE* **2010**, *7660* (May), 766011.
(101) Fang, Y.; Armin, A.; Meredith, P.; Huang, J. Accurate Characterization of Next-Generation Thin-Film Photodetectors. *Nat. Photonics* **2019**, *13*, 1.

https://dx.doi.org/10.1021/acsphotonics.0c01068
ACS Photonics XXXX, XXX, XXX−XXX